The multiband effective-mass model of the electronic structure and intersubband absorption in p-type-doped twinning superlattices

1999 J. Phys.: Condens. Matter 11 6891

(http://iopscience.iop.org/0953-8984/11/36/307)

J. Phys.: Condens. Matter **11** (1999) 6891–6909. Printed in the UK PII: S0953-8984(99)02557-6

The multiband effective-mass model of the electronic structure and intersubband absorption in p-type-doped twinning superlattices

M Tadić and Z Ikonić

Faculty of Electrical Engineering, University of Belgrade, PO Box 3554, Belgrade 11120, Yugoslavia

Received 10 March 1999

Abstract. The electronic structure and the infrared light absorption in p-doped twinning superlattices are calculated. The standard 6×6 $\boldsymbol{k} \cdot \boldsymbol{p}$ Hamiltonian is employed, with the split-off band taken into account. The effective scattering potential at the twinning interface is modelled by appropriate δ-potentials. The calculation of the intersubband absorption is also performed. The origin of each absorption peak is identified, and the polarization dependence is explained in terms of the structural parameters. The magnitude of the absorption coefficient indicates considerable benefits offered solely by the change of the atomic stacking sequence, i.e. the enhanced scattering related to it. Good agreement between our results and those computed by the pseudopotential theory is found.

1. Introduction

There has been growing interest in microstructures consisting of differently oriented semiconductors in recent years [1], a special class of these being twinning superlattices (TSLs) [2,3]. A single twinning boundary (STB) is a common defect in semiconductors, which detrimentally affects electron transport in a device. However, if the twinning boundary is periodically repeated, coherent scattering induces the continuum in both the valence and the conduction band to split into a set of minibands. This means that electronic, transport, and optical properties are all affected by twinning. The TSL is currently known to occur in some natural crystals [4], amorphized Ge films [5], and artificially grown whiskers [6], and very recently a Si-based TSL was successfully produced by boron-mediated epitaxial growth [7]. It should be stressed that peculiarities of the electronic structure occur due to the rotation-induced change of Bloch functions across the boundary. The electronic properties of a STB or TSL may be obtained by microscopic methods—pseudopotential, tight binding and suchlike—because these recognize the detailed atomic configuration and structure of the wave functions. It is less clear, however, whether a simpler method like that of multiband effective-mass theory (EMT) [8] would be able to handle these structures. Its ability to do so would be welcomed for at least two reasons. One is that the computational complexity and related numerical problems in microscopic methods are grossly reduced in EMT-based approaches. The second is that, while microscopic methods may give reasonably accurate band structures in the $\sim$10 eV range, it may be very difficult to get them to accurately reproduce fine details of the band structure in a narrow range of energies which may be of greatest interest for a particular problem. Indeed the commonly used sets of pseudopotential or tight-binding parameters usually fail to deliver the bulk effective mass or

0953-8984/99/366891+19$30.00

Luttinger parameters with good accuracy. A closer look at electron scattering in a twinning interface indicates two sources of this phenomenon: the fact that the two bulks are different (in their crystallographic orientation), and the fact that the atomic stacking sequence in the vicinity of the interface, and hence also the associated microscopic potential, are not bulk-like. The EMT method, if comprehensive enough, may sense the crystal orientation, but it may not be expected to account accurately, if at all, for the interface microscopic potential. This latter should therefore be built in EMT as an effective interface potential which acts upon envelope wave functions. The p-like hole states are far more affected by twinning than are s-like conduction band states in a direct-gap semiconductor, and clearly only the former should be explored in this respect.

In this paper an EMT-based model of the electronic structure and intersubband absorption between the valence minibands in the TSL is devised. The model relies on the results of the pseudopotential theory [3] in deriving some of its parameters (interface effective potentials, which are modelled by δ-function potentials positioned at the interface, with different strengths for the three hole branches). In order to obtain the exact potential, quite extensive density functional theory [9] should in principle be employed, but the simple model used is found to be quite acceptable. We allow that the in-plane inversion asymmetry of the TSL's semiconductor influences the two-dimensional electron gas (2DEG), and do not impose any additional symmetry other than the host crystal's own. Then we proceed to calculate the intersubband optical absorption, via finding the interaction Hamiltonian, and transition matrix elements. The dependence of the absorption on the light polarization is attributed to the specific configuration of the transition matrix elements delivered by the interaction Hamiltonian in this system. Certainly the theory devised for TSLs is also applicable for a single twinning boundary, as a large-period limit of a TSL, and should enable one to study hole scattering, excitons, and other phenomena thereby.

The paper is organized as follows. In section 2 the theory of the electronic structure is presented and described in detail. The eigenfunctions from this part are then used in section 3 to calculate matrix elements and the absorption coefficient. The peculiarities of the miniband structure and the dependence of the absorption on the light polarization and TSL parameters are discussed in section 4.

2. Electronic structure

We start from the multiband EM Hamiltonian in the $|J, m_J\rangle$ basis:

$$|3/2, 3/2\rangle, |3/2, 1/2\rangle, |3/2, -1/2\rangle, |3/2, -3/2\rangle, |1/2, 1/2\rangle, |1/2, -1/2\rangle$$

spanning heavy holes, light holes, and the split-off band, with the energy axis pointing downwards [10]:

$$H = \frac{\hbar^2}{2m_0}\begin{bmatrix} A_+ & B & C & 0 & \frac{1}{\sqrt{2}}B & \sqrt{2}C \\ B^\dagger & A_- & 0 & C & -\sqrt{2}Q & -\sqrt{\frac{3}{2}}B \\ C^\dagger & 0 & A_- & -B & -\sqrt{\frac{3}{2}}B^\dagger & \sqrt{2}Q \\ 0 & C^\dagger & -B^\dagger & A_+ & -\sqrt{2}C^\dagger & \frac{1}{\sqrt{2}}B^\dagger \\ \frac{1}{\sqrt{2}}B^\dagger & -\sqrt{2}Q & -\sqrt{\frac{3}{2}}B & -\sqrt{2}C & A_\Delta & 0 \\ \sqrt{2}C^\dagger & -\sqrt{\frac{3}{2}}B^\dagger & \sqrt{2}Q & \frac{1}{\sqrt{2}}B & 0 & A_\Delta \end{bmatrix} \tag{1}$$

where

$$\begin{aligned} A_{\pm} &= P_{\mathrm{h}} \pm Q_{\mathrm{h}} & A_{\Delta} &= P_{\mathrm{h}} + \Delta \\ P_{\mathrm{h}} &= \gamma_1(k_x^2 + k_y^2 + k_z^2) & Q_{\mathrm{h}} &= \gamma_3(k_x^2 + k_y^2 - 2k_z^2) \end{aligned} \tag{2}$$

and

$$\begin{aligned} B &= \sqrt{\frac{2}{3}}(\gamma_2 - \gamma_3)k_+^2 - \frac{2}{\sqrt{3}}(2\gamma_2 + \gamma_3)k_- k_z \\ C &= -\frac{\gamma_2 + 2\gamma_3}{\sqrt{3}}k_-^2 + 2\sqrt{\frac{2}{3}}(\gamma_2 - \gamma_3)k_+ k_z \\ k_+ &= k_x + \mathrm{i}k_y \qquad k_- = k_x - \mathrm{i}k_y. \end{aligned} \tag{3}$$

Here k_x, k_y, and k_z denote the hole wave-vector components in the coordinate system oriented along the $[11\bar{2}]$, $[\bar{1}10]$, and [111] crystallographic directions [11], respectively, γ_1, γ_2, and γ_3 are the Luttinger parameters, Δ the spin–orbit splitting, and m_0 the free-electron mass. In 2D microstructures, the kinetic Hamiltonian given by equation (1) takes an operator form, with $k_z \to -\mathrm{i}\,\partial/\partial z$ for the superlattice oriented along [111], and is accompanied by a macroscopic potential; these act together on the envelope function vector $F(z)$:

$$(H + V(z))F(z) = EF(z) \tag{4}$$

where the energy E is measured from the valence band top downwards. The structure under consideration comprises a sequence of oppositely oriented (mutually twisted by π radians about the z-axis) slabs having l and m monolayers of a single semiconductor X (=GaAs, Ge, Si). It may be conveniently denoted as $\mathrm{X}_l\mathrm{X}'_m$, and is symbolically depicted in figure 1. The Hamiltonian given by equation (1) is used for the material of (say) orientation ↑, and more precisely denoted as $H_{\uparrow}$, whereas an appropriate form should be constructed for the (rotated) layer ↓. Now, we first note that the transversal invariance is preserved in the layer planes, so the transversal wave vector $\boldsymbol{k}_{\mathrm{t}} = (k_x, k_y)$ is a good quantum number for the whole structure and the wave functions should behave as $\exp(\mathrm{i}\boldsymbol{k}_{\mathrm{t}} \cdot \boldsymbol{r}_{\mathrm{t}})$ in both layers. If one imagines that a part of the crystal is rotated by π radians about the z-axis, its Hamiltonian and a state behaving as $\exp(\mathrm{i}\boldsymbol{k}_{\mathrm{t}} \cdot \boldsymbol{r}_{\mathrm{t}})$ will be unchanged in its own, rotated coordinate system. However, the wave-function matching should be performed in a common coordinate system. Hence, to make the Hamiltonian analogous to (1) but for the rotated crystal, we first set the Hamiltonian

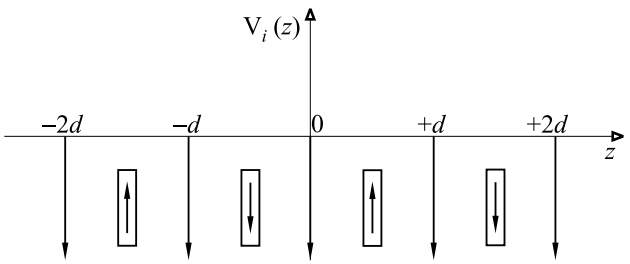

Figure 1. A schematic view of the twinning superlattice having two layers of equal width d. Two parts of the period are mutually twisted by π radians, and there is a δ-potential V_i for each basis state (i = HH, LH, SO). Layer ↑ is considered as the normal with the Brillouin zone k_x-, k_y-, and k_z-axes directed along $[11\bar{2}]$, $[\bar{1}10]$, and [111] crystallographic directions, respectively. The same Hamiltonian applies to the rotated layer (↓), but in the coordinate system defined by unit vectors oriented in the $[\bar{1}\bar{1}\bar{2}]$, $[1\bar{1}0]$, and [111] directions.

for the normal crystal but with $\boldsymbol{k}_t \to -\boldsymbol{k}_t$, and then rotate the crystal (which will restore the $\exp(i\boldsymbol{k}_t \cdot \boldsymbol{r}_t)$ behaviour in the unrotated coordinate system). However, rotation also affects the basis functions with $m_J = \pm 3/2, \pm 1/2$, so we also have to change to the 'old' basis set, as defined for the unrotated crystal, by applying the rotation matrix $\tilde{R}$ which in this case reads

$$\tilde{R} = \mathrm{diag}(-i, +i, -i, +i, +i, -i). \tag{5}$$

Therefore

$$H_\downarrow(k_t) = \tilde{R} H_\uparrow(-k_t) \tilde{R}^{-1} \tag{6}$$

is the appropriate Hamiltonian for the (rotated) layer $\downarrow$ (note that the k_z-component of the wave vector is not changed by this rotation). In effect, the elements of $H_\uparrow$, equation (1), which change in this operation are B and C, i.e.

$$\begin{aligned} B_\downarrow &= -\sqrt{\frac{2}{3}}(\gamma_2 - \gamma_3)k_+^2 - \frac{2}{\sqrt{3}}(2\gamma_2 + \gamma_3)k_- k_z \\ C_\downarrow &= -\frac{\gamma_2 + 2\gamma_3}{\sqrt{3}}k_-^2 - 2\sqrt{\frac{2}{3}}(\gamma_2 - \gamma_3)k_+ k_z. \end{aligned} \tag{7}$$

The 6×6 Hamiltonian given by equation (1) suffers from relative complexity, which is frequently alleviated by making additional assumptions about the symmetry of the electronic structure, the most successful being the axial approximation. In essence it neglects the effects of the corrugation of constant-energy lines in the $\boldsymbol{k}_t$-plane, and enables a rather straightforward block diagonalization of the Hamiltonian, which halves the size of the problem. In compositional superlattices the axial approximation is known to work best in the [111] direction [11], which is encountered in TSLs. However, the crystal rotation is one of the major effects bringing about miniband structure in TSLs; hence the axial approximation would here be of doubtful validity, so it was not used in this work. Indeed, as we show below, introducing the axial approximation *a posteriori* leads to considerable errors.

The empirical pseudopotential method (EPM) for a single twinning boundary indicates the existence of hole bound states and resonances, localized at the interface [3]. These originate from the feature that the microscopic potential in the vicinity of the interface is essentially different from the potential in either rotated or unrotated bulk. Since the EPM, like other microscopic methods, recognizes the microscopic structure, it is able to discover such states. The EMT, however, should not be expected to do so, and indeed we have checked that direct application of $H_\uparrow$ and $H_\downarrow$ to a single twinning interface gives no bound states or resonances. Since these states are generally important for electronic and optical properties, the EMT Hamiltonian should be amended with an 'effective' interface potential.

Both the EPM and self-consistent pseudopotential calculations indicate that the non-bulk-like perturbation of the microscopic potential at the interface has a very short range ($\sim$one lattice constant or so) [12]. Alternatively, in the atomic stacking sequence ABCAB$\hat{\mathrm{C}}$BACBA one may recognize the B$\hat{\mathrm{C}}$B wurtzite slab 'inserted' in zinc-blende material, and recall that band discontinuity appears at the zinc-blende/wurtzite interface, as discussed in more detail in [13]. The sign of the discontinuity is indeed such that holes tend to be confined to the wurtzite layer, i.e. the twinning boundary, though it is not clear whether the concept of band discontinuity, and its value derived for the junction of two slabs, is quantitatively applicable to a layer as thin as this. In any case, bound states are not found from the EMT Hamiltonian, equation (4), with $V(z) = 0$. The simplest model potential for amending the EMT Hamiltonian would be an attractive (negative-strength) Dirac δ-function centred at the interface. A similar idea was employed to describe Γ–X-valley mixing at interfaces [14]. Its strength should be determined by comparison to EPM results. However, we find that a single δ-potential cannot

even approximately reproduce the EPM results. (Ge and Si have one HH and one LH bound state, above the valence band top, while GaAs additionally has an SO-like resonance slightly above the SO band top, weakly coupled to the valence band continuum via SO–LH mixing.) This may be an indication that the δ-function should be replaced by a finite-range potential, the shape of which is to be determined in the same way (though it could not be done uniquely, then). We have chosen, instead, to keep the model potential as simple as possible, and have set three δ-function potentials at the interface with different strengths for the three hole branches, determined so as to match the EPM-calculated state energies of the STB. The resulting strengths are given in table 1. These are calculated from the EPM-predicted bound-state energies of the single twinning boundary at $k_t = 0$ and the hole effective masses, according to

$$V_{\mathrm{HH}} = 2\left[\frac{2m_0}{\hbar^2}(\gamma_1 - 2\gamma_3)|\tilde{E}_{\mathrm{HH}}|\right]^{1/2} \tag{8}$$

$$V_{\mathrm{LH}} = 2\left[\frac{2m_0}{\hbar^2}(\gamma_1 + 2\gamma_3)|\tilde{E}_{\mathrm{LH}}|\right]^{1/2} \tag{9}$$

$$V_{\mathrm{SO}} = 2\left(\frac{2m_0}{\hbar^2}\gamma_1|\tilde{E}_{\mathrm{SO}} - \Delta|\right)^{1/2}. \tag{10}$$

The LH–SO band coupling was in this instance neglected, as the EPM calculation indicated that this was rather weak. The interface effective potential is thus a diagonal matrix which, in the case of TSLs with $l = m$, for instance, has the Dirac comb form:

$$V(z) = \frac{\hbar^2}{2m_0}V_\delta \sum_{i=-\infty}^{+\infty} \delta(z - \mathrm{i}d) \tag{11}$$

with d denoting a half of the superlattice period, and V_δ is given by

$$V_\delta = \mathrm{diag}(V_{\mathrm{HH}}, V_{\mathrm{LH}}, V_{\mathrm{LH}}, V_{\mathrm{HH}}, V_{\mathrm{SO}}, V_{\mathrm{SO}}). \tag{12}$$

As we find by calculation, the EPM results are reproduced reasonably well not only for a single twinning boundary, but for TSLs too [3]. Therefore we believe that this form of effective interface potential, different for HH, LH, and SO branches, is not very unusual—recall that

Table 1. Material parameters of GaAs, Ge, and Si, and for a single twinning interface, determined by experiment ($\mathcal{E}$), and extracted from the empirical pseudopotential theory ($\mathcal{T}$) [2,3]. The Luttinger parameters (γ_1, γ_2, and γ_3), indices of refraction n, spin–orbit splitting energies Δ, lattice constants a, and the strengths of interface δ-potentials for different bulk states (V_{HH}, V_{LH}, V_{SO}), as computed from energies of bound/resonant states in a single twinning boundary ($\tilde{E}_{\mathrm{HH}}$, $\tilde{E}_{\mathrm{LH}}$, $\tilde{E}_{\mathrm{SO}}$) and values of the γ-parameters either experimental or implicit in the EPM, are all given.

Parameter	GaAs, $\mathcal{E}$	GaAs, $\mathcal{T}$	Ge, $\mathcal{E}$	Ge, $\mathcal{T}$	Si, $\mathcal{E}$	Si, $\mathcal{T}$
γ_1	6.85	5.57	13.35	7.40	4.22	6.10
γ_2	2.10	1.78	4.25	2.30	0.39	1.10
γ_3	2.90	2.28	5.69	3.10	1.44	2.20
$\tilde{E}_{\mathrm{HH}}$ (meV)	—	−19	—	−25.8	—	−45.6
$\tilde{E}_{\mathrm{LH}}$ (meV)	—	−0.3	—	−0.5	—	−3.5
$\tilde{E}_{\mathrm{SO}} - \Delta$ (meV)	—	−0.65	—	—	—	—
V_{HH} (nm^{-1})	−1.45	−1.42	−2.31	−1.80	−2.53	−2.85
V_{LH} (nm^{-1})	−0.608	−0.546	−1.08	−0.806	−1.41	−1.96
V_{SO} (nm^{-1})	−0.648	−0.617	0	0	0	0
n	3.6	—	4.0	—	3.43	—
Δ (meV)	340	333	282	278	44	43
a (nm)	0.565325	—	0.56579	—	0.543095	—

e.g. Γ- and X-valley electrons experience quite different macroscopic potentials at GaAs/AlAs interfaces while the microscopic potential is clearly unique. Generally, the interface potential may be a full matrix, i.e. not necessarily diagonal, provided that it remains Hermitian. It should be filled in with matrix elements of the *effective*, that is state-dependent, potential, because it acts only upon the envelope wave functions and not upon the microscopic wave functions. This implies that all the matrix elements may also depend on k_t. However, to keep the model as simple as possible we attempted to use the diagonal-matrix form of the potential, the elements of which depend on the type of holes but not on k_t. The validity of this approximation had to be checked by comparing against the EPM results, and we found that it does indeed provide reasonable accuracy.

The calculation of the miniband structure starts with diagonalization of the Hamiltonian (1) in order to obtain the dispersion $k_z(E)$. The Hamiltonian is not invariant under the in-plane π-radian rotation; thus in each layer a set of six k_z-values is to be determined (there is no $\pm k_z$-degeneracy for the [111] direction). Degenerate eigenvectors corresponding to the same k_z are alternately arranged as the subsequent columns of the matrices X and Y, and the procedure is repeated for all k_z. In order to increase the stability of the procedure, the first row in X and the second row in Y are set equal to 0, as in [15]. The eigenproblem for the superlattice is then solved by matching the wave functions (written as linear combinations of bulk states) and the probability current density across the interface, and imposing the Bloch conditions. It turns out that the complexity of the original problem of finding the zero of the 24×24 determinant may be reduced twice if the original secular matrix is conveniently partitioned, as

$$S = \begin{bmatrix} P - R & Q \\ (P + R)E_{2\uparrow}(+d) & \mathrm{e}^{\mathrm{i}2qd} Q E_{2\uparrow}(-d) \end{bmatrix} \tag{13}$$

where

$$P = \begin{bmatrix} X_\uparrow & Y_\uparrow \\ D_{\mathrm{eff}} X_\uparrow + X_\uparrow G_{2\uparrow}(0) & D_{\mathrm{eff}} Y_\uparrow + Y_\uparrow G_{2\uparrow}(0) \end{bmatrix} \tag{14}$$

$$R = \begin{bmatrix} 0 & 0 \\ D_\delta X_\uparrow & D_\delta Y_\uparrow \end{bmatrix} \tag{15}$$

and

$$Q = \begin{bmatrix} -X_\downarrow & -Y_\downarrow \\ -X_\downarrow G_{2\downarrow}(0) & -Y_\downarrow G_{2\downarrow}(0) \end{bmatrix} \tag{16}$$

where q denotes the superlattice wave vector.

We seek a solution of the system $Sc = 0$ where $c = [c_\uparrow, c_\downarrow]^{\mathrm{T}}$ are the coefficients of expansion of the envelope functions in the k_z-modes. The matrices D_{eff} and D_δ are given in appendix A, while $E_{2\uparrow}(z)$ and $E_{2\downarrow}(z)$ are given by

$$E_{2\uparrow}(z) = \begin{bmatrix} E_\uparrow(z) & 0 \\ 0 & E_\uparrow(z) \end{bmatrix} \qquad E_{2\downarrow}(z) = \begin{bmatrix} E_\downarrow(z) & 0 \\ 0 & E_\downarrow(z) \end{bmatrix} \tag{17}$$

respectively, where $E_\uparrow(z)$ and $E_\downarrow(z)$ are diagonal matrices made up of the plane-wave functions:

$$E_{\uparrow ij}(z) = \mathrm{e}^{\mathrm{i}k_{z\uparrow i} z}\delta_{ij} \qquad E_{\downarrow ij}(z) = \mathrm{e}^{\mathrm{i}k_{z\downarrow i} z}\delta_{ij}. \tag{18}$$

Here δ_{ij} denotes the Kronecker delta symbol. Similarly,

$$G_{2\uparrow}(z) = \begin{bmatrix} G_\uparrow(z) & 0 \\ 0 & G_\uparrow(z) \end{bmatrix} \qquad G_{2\downarrow}(z) = \begin{bmatrix} G_\downarrow(z) & 0 \\ 0 & G_\downarrow(z) \end{bmatrix} \tag{19}$$

where $G_\downarrow(z)$ and $G_\downarrow(z)$ denote diagonal matrices:

$$G_{\uparrow ij}(z) = \mathrm{i}k_{z\uparrow i}\mathrm{e}^{\mathrm{i}k_{z\uparrow i} z}\delta_{ij} \qquad G_{\downarrow ij}(z) = \mathrm{i}k_{z\downarrow i}\mathrm{e}^{\mathrm{i}k_{z\downarrow i} z}\delta_{ij} \tag{20}$$

respectively. We follow the prescription of [16], suggesting the application of subblock pivoting to equation (13), and reducing the problem to a Hermitian one. In addition to leading to a more tractable model, this method shows its superiority to the non-reduced scheme. More specifically, the main drawback of equation (13) is the existence of spurious solutions [17], created by hole wave vectors beyond the Brillouin zone. Their adverse effects are readily removed by making suitable linear combinations of the matrix elements. If the exponential functions in equation (13) are replaced by tangents, inherently stable solutions may be guaranteed provided that the reshuffling of S, equation (13), is properly done [16]:

$$\tilde{S} = \begin{bmatrix} PC_q + \mathrm{i}RS_q & QC_k \\ -\mathrm{i}PS_q - RC_q & \mathrm{i}QS_k \end{bmatrix} \tag{21}$$

where C_q, S_q, C_k, and S_k are given by

$$C_q = \frac{\mathrm{e}^{-\mathrm{i}qd}E_{2\uparrow}(+d/2) + \mathrm{e}^{+\mathrm{i}qd}E_{2\uparrow}(-d/2)}{2} \tag{22}$$

$$S_q = \frac{\mathrm{e}^{-\mathrm{i}qd}E_{2\uparrow}(+d/2) - \mathrm{e}^{+\mathrm{i}qd}E_{2\uparrow}(-d/2)}{2\mathrm{i}} \tag{23}$$

$$C_k = \frac{E_{2\downarrow}(+d/2) + E_{2\downarrow}(-d/2)}{2} \tag{24}$$

$$S_k = \frac{E_{2\downarrow}(+d/2) - E_{2\downarrow}(-d/2)}{2\mathrm{i}} \tag{25}$$

respectively. Furthermore, we define

$$T_k = C_k S_k^{-1} \qquad T_q = C_q S_q^{-1}. \tag{26}$$

As they are generally non-singular, either subblock in the second column of equation (21) may be used as the pivot. If S_{12} is employed for that purpose, the characteristic equation reads

$$S_{\mathrm{c}}c_{\mathrm{c}} = \begin{bmatrix} I + \mathrm{i}RT_qP^{-1} & QC_k \\ \mathrm{i}QT_kQ^{-1} - QT_kQ^{-1}RT_qP^{-1} + \mathrm{i}PT_qP^{-1} + RP^{-1} & 0 \end{bmatrix} \begin{bmatrix} c_{\mathrm{c}\uparrow} \\ c_{\mathrm{c}\downarrow} \end{bmatrix} = [0] \tag{27}$$

where S_{c} denotes the 2×2-subblock matrix, $c_{\mathrm{c}} = [c_{\mathrm{c}\uparrow}, c_{\mathrm{c}\downarrow}]^{\mathrm{T}}$ are the coefficients of the transformed basis states, and $[0]$ is the 24×1 zero matrix. The S_{12}-subblock, however, may become a singular matrix at some energy; hence the electronic structure found from equation (27) may lack some eigenvalues. The latter are efficiently regained from the characteristic equation obtained with the S_{22}-subblock as a pivot:

$$S_{\mathrm{s}}c_{\mathrm{s}} = \begin{bmatrix} -QT_k^{-1}Q^{-1} + \mathrm{i}QT_k^{-1}Q^{-1}RT_q^{-1}P^{-1} - PT_qP^{-1} - \mathrm{i}RP^{-1} & 0 \\ -\mathrm{i}I - RT_q^{-1}P^{-1} & \mathrm{i}QS_k \end{bmatrix} \begin{bmatrix} c_{\mathrm{s}\uparrow} \\ c_{\mathrm{s}\downarrow} \end{bmatrix} = [0] \tag{28}$$

where S_{s} and c_{s} are matrices consisting of 2×2 and 2×1 subblocks, respectively. It is clear from equations (27) and (28) that only $S_{\mathrm{c}21}$ and $S_{\mathrm{s}11}$ are to be considered for eigenvalue determination. When the solution is obtained, the corresponding system of equations is solved in order to find the $c_{\mathrm{c,s}\uparrow}$-coefficients, whereas $c_{\mathrm{c,s}\downarrow}$-coefficients are found from the remaining row in the secular equation, i.e. the first row in S_{c} and the second row in S_{s}. In order to express the eigenfunctions in terms of bulk plane waves, backward transformations should be carried out:

$$c = \tilde{B}^{-1}A_{\mathrm{c}}^{-1}c_{\mathrm{c}} \tag{29}$$

or

$$c = \tilde{B}^{-1}A_{\mathrm{s}}^{-1}c_{\mathrm{s}} \tag{30}$$

where

$$A_{\mathrm{c}} = \begin{bmatrix} PC_q & 0 \\ 0 & I \end{bmatrix} \qquad A_{\mathrm{s}} = \begin{bmatrix} PS_q & 0 \\ 0 & I \end{bmatrix} \tag{31}$$

and

$$\tilde{B} = \begin{bmatrix} E_{2\uparrow}(+d/2)\mathrm{e}^{\mathrm{i}qd} & 0 \\ 0 & E_{2\downarrow}(-d/2) \end{bmatrix}. \tag{32}$$

Multiplying c by the bulk eigenvectors X and Y, the envelope functions may be expressed as

$$F_{\uparrow}(z) = W_{\uparrow}E_{1\uparrow}(z) \qquad F_{\downarrow}(z) = W_{\downarrow}E_{1\downarrow}(z) \tag{33}$$

in the $\uparrow$ and $\downarrow$ layer, respectively, where $E_{1\uparrow}$ and $E_{1\downarrow}$ denote one-dimensional arrays of exponentials in $E_{\uparrow}$ and $E_{\downarrow}$, i.e.

$$E_{1\uparrow i} = \mathrm{e}^{\mathrm{i}k_{z\uparrow i}z} \qquad E_{1\downarrow i} = \mathrm{e}^{\mathrm{i}k_{z\downarrow i}z} \tag{34}$$

and matrices $W_{\uparrow}$ and $W_{\downarrow}$ are composed according to

$$W_{\uparrow ij} = (c_{\uparrow j}X_{\uparrow ij} + c_{\uparrow(j+6)}Y_{\uparrow ij}) \tag{35}$$

$$W_{\downarrow ij} = (c_{\downarrow j}X_{\downarrow ij} + c_{\downarrow(j+6)}Y_{\downarrow ij}) \tag{36}$$

respectively.

3. Intersubband absorption

The simplest way to derive the transition matrix element connecting two states is to find the gradient of the starting Hamiltonian, equation (1), in $\boldsymbol{k}$-space [18, 19], even though an alternative procedure has been proposed [20]. The interaction Hamiltonian thus obtained (scaled by the product of the electron charge and magnetic vector potential) may be conveniently separated into an overlap matrix and a dipole matrix. For each polarization of the plane-polarized light, there is a particular combination of the envelope functions $F(z)$ which provides an absorption coefficient in excess of the free-hole absorption coefficient. Matrix elements of the interaction Hamiltonian (divided by $\hbar/2m_0$) are given in table B1 in appendix B. Using these and the expression for the envelope functions, equations (33), the transition matrix elements connecting the initial (i) and the final (f) state for light polarized along $m = x, y, z$ reads

$$\begin{aligned} M_{fi}^{(m)} &= \int_{-d}^{0} E_{1\downarrow f}^{\dagger}(z)W_{\downarrow f}^{\dagger}H_{\mathrm{int}}^{\downarrow(m)}W_{\downarrow i}E_{1\downarrow i}(z)\,\mathrm{d}z + \int_{0}^{+d} E_{1\uparrow f}^{\dagger}(z)W_{\uparrow f}^{\dagger}H_{\mathrm{int}}^{\uparrow(m)}W_{\uparrow i}E_{1\uparrow i}(z)\,\mathrm{d}z \\ &\quad + \int_{-d}^{d} E_{1f}^{\dagger}(z)W_{f}^{\dagger}\frac{k_z(\mathcal{I})}{2}W_i E_{1i}(z)\,\mathrm{d}z \\ &= \sum_{l=1}^{6}\sum_{j=1}^{6}\left[M_{\mathrm{W}lj}^{\uparrow}\frac{\mathrm{e}^{\mathrm{i}(k_{z\uparrow j}-k_{z\uparrow l}^{*})d}-1}{\mathrm{i}(k_{z\uparrow j}-k_{z\uparrow l}^{*})} + M_{\mathrm{W}lj}^{\downarrow}\frac{1-\mathrm{e}^{-\mathrm{i}(k_{z\downarrow j}-k_{z\downarrow l}^{*})d}}{\mathrm{i}(k_{z\downarrow j}-k_{z\downarrow l}^{*})}\right] + M_{\mathrm{W}}^{\mathcal{I}} \end{aligned} \tag{37}$$

where H_{int} indicates the interaction Hamiltonian without interface elements, and $k_z(\mathcal{I})/2$ denotes the remaining interface part, where $\mathcal{I}$ is given in table B1. $M_{\mathrm{W}}^{\uparrow}$ and $M_{\mathrm{W}}^{\downarrow}$ indicate the products of the three middle terms in the first and the second integral in this expression, respectively, and $M_{\mathrm{W}}^{\mathcal{I}}$ the interface matrix element.

For the absorption coefficient, a rather general formula is used [21]:

$$\alpha(\hbar\omega) = \frac{\tilde{C}}{\Omega}\sum_{i}\sum_{f}\left|\frac{\hbar}{2m_0}M_{fi}\right|^2\frac{\Gamma/2\pi}{(E_f - E_i - \hbar\omega)^2 + \Gamma^2/4}(f_{\mathrm{FD}}(E_i) - f_{\mathrm{FD}}(E_f)). \tag{38}$$

Here f_{FD} denotes the Fermi–Dirac distribution function for holes. The constant $\tilde{C}$ is given by

$$\tilde{C} = \frac{\pi e^2}{nc\epsilon_0\omega}$$

where e denotes the electron charge, n the index of refraction, c the speed of light, ϵ_0 the vacuum permittivity, and $\overline{h}\omega$ the photon energy. In equation (38) Ω denotes the volume of the structure (superlattice unit cell) and Γ the full width of the line-broadening Lorentzian. Applying cyclic boundary conditions we finally get

$$\alpha(\overline{h}\omega) = \frac{e^2\overline{h}}{8\pi^2 c\epsilon_0}\frac{1}{n\overline{h}\omega}\int_{-\infty}^{+\infty}\mathrm{d}k_x\int_{-\infty}^{+\infty}\mathrm{d}k_y\int_{-\pi/2d}^{+\pi/2d}\mathrm{d}q\sum_i\sum_f\left|\frac{\overline{h}}{2m_0}M_{fi}\right|^2 \times \frac{\Gamma/2\pi}{(E_f - E_i - \overline{h}\omega)^2 + \Gamma^2/4}(f_{\mathrm{FD}}(E_i) - f_{\mathrm{FD}}(E_f)). \tag{39}$$

Here, $|M_{fi}|^2$ is obtained by summing over the four possible transitions offered by the double degeneracy of the initial (i) and the final (f) state.

4. Results and discussion

The theory described in the previous sections is applied to GaAs-, Ge-, and Si-based TSLs. We consider a symmetric ($l = m$) TSL, with the half-period of $m = 9$ monolayers, which for GaAs amounts to $d = 2.9$ nm. We assume homogeneous doping of $N_{\mathrm{A}} = 10^{17}$ cm^{-3} acceptors throughout the structure (as in [3]). The absorption coefficient is calculated at $T = 77$ K. For the homogeneous relaxation time we assume 0.1 ps, which corresponds to the Lorentzian width of $\Gamma = 13.16$ meV. The Luttinger parameters [22, 23], the eigenenergies of the STBs, the strengths of the delta potentials, and other relevant parameters [22] for the three semiconductors are shown in table 1. The eigenenergies do not depend on the sign of k_x, k_y, or q, but the eigenfunctions are neither invariant nor simply transformed under the inversion symmetry. The region of important states for optical transitions is taken to be bounded by perpendicular planes intersecting at $(k_x, k_y, q) = (\pm 0.5, \pm 0.5, \pm\pi/2d)$ (in units of nm^{-1}), and is subdivided into $13 \times 13 \times 17$ cubes. These 2873 points provide a sufficiently dense mesh for the calculation of the absorption coefficient, and include all states of relevance. This is due to the rather low values of the Fermi level (table 2), implying that just a fraction of the whole 2D Brillouin zone is populated. One may argue against low doping levels, but we select the same value as in [3] for the purpose of comparison between the EMT and EPM [3] calculation. In addition, the self-consistency effects are neglected in the present calculations.

Table 2. Zone-centre energies of the four lowest minibands and Fermi levels (with the energy axis pointing downwards) corresponding to a hole density of 10^{17} cm^{-3} at $T = 77$ K, calculated from the EPM ($\mathcal{T}$) and the multiband EMT with the experimental values of the γ-parameters ($\mathcal{E}$), and those extracted from pseudopotential theory ($\mathcal{P}$).

Level	GaAs, $\mathcal{T}$	GaAs, $\mathcal{E}$	GaAs, $\mathcal{P}$	Ge, $\mathcal{T}$	Ge, $\mathcal{E}$	Ge, $\mathcal{P}$	Si, $\mathcal{T}$	Si, $\mathcal{E}$	Si, $\mathcal{P}$
E_1 (meV)	−27	−27.1	−26.8	−35	−40.8	−35.0	−61	−56.1	−59.6
E_2 (meV)	−7	−8.19	−7.35	−10	−14.6	−10.9	−30	−27.4	−29.6
E_3 (meV)	−6	−0.681	−1.73	−7	14.0	−6.76	−13	−21.2	−18.6
E_4 (meV)	39	45.8	44.0	52	85.7	52.2	35	44.0	44.0
E_F (meV)	—	−41.1	−41.7	—	−46.8	−47.2	—	−70.3	−70.1

The electronic structure is calculated with commonly used (experimental) Luttinger parameters, and those derived by fitting pseudopotential dispersion curves to the effective-mass dispersions (i.e. implicit in EPM calculations) [3], the latter being useful mainly for

comparison of EPM and EMT results. Generally, we found very good agreement between the three calculations, which may be noticed from table 2, where the energies of the four lowest minibands in the centre of the 2D Brillouin zone are shown. It may be noticed that the errors introduced by the EMT are lowest for two ground minibands of heavy and light holes, as is indeed expected [24]. Small values of these errors justify the use of the interface δ-potential in the matrix form, equation (8). As an example, the HH ground-state energy in GaAs is fairly well estimated by the EMT. The discrepancy between the EMT and EPM becomes negligible if the Luttinger parameters are extracted from the EPM itself, which does not seem surprising, since the fit to the dispersion relation of the EMT works best for the lowest-energy states [24]. Excellent agreement between the EPM and EMT was found for Ge, whereas treatment of Si by EMT produces a larger error, which may be accounted for by the more complex band structure found in this semiconductor.

For the second miniband, the accuracy of EMT is generally lower than for the first miniband, but EMT results still depart by just a few meV from the EPM ones. For the third and the fourth level the discrepancy is much larger; therefore one may question the validity of the effective-mass theory. This finding matches the general conclusion reached in [24] for GaAs/AlAs superlattices. A large deviation may be explained as due to either a limited basis of bulk states or too simple a model for the effective interface potential. It is difficult to estimate the relative importance of the two approximations. Nonetheless, we consider the deviations of the zone-centre energies of the order of a few meV acceptable, keeping in mind that the EPM in its different implementations (interface matching or supercell) does not really offer accuracy much better than that. Furthermore, zero energy gaps at $k_t = 0$, as well as the miniband folding effect found from the EPM, are also yielded by EMT calculation, as clearly depicted in figure 2.

Superlattice eigenstates are classified according to the bulk states that they are composed of. These are denoted in figure 2 as heavy hole (HH) and light hole (LH), the latter being shorthand notation for the mixture of light-hole and split-off bands (LH + SO). The second miniband composed of LH + SO states clearly has a smaller effective mass than the ground miniband, thus having a large width. Furthermore, since HH and LH states do not mix at $k_t = 0$, LH1 and LH2 states cross HH minibands, at four points in this example, while the narrower LH3 and LH4 minibands do that just twice, as displayed in figure 2. As expected, HH minibands do not cross; they are well separated, and their widths increase with the miniband index. In contrast, LH4 and LH5 states exhibit clear anticrossing behaviour near $\Delta = 340$ meV. All crossings at $k_t = 0$ are converted to anticrossings, and also the zero energy gaps disappear at finite k_t in all three semiconductors. As an example, such behaviour in GaAs at $q = 0$ is displayed in figure 3. There exists a prominent anticrossing between the first and the second miniband, and a much smaller effect of this kind occurs between the ninth and tenth miniband, while it seems that the remaining ones do not exchange their effective masses anywhere in the $\boldsymbol{k}_t$-plane. One should note the existence of almost dispersionless fifth and sixth minibands, both of them being heavy hole in character. Even though the underlying crystal structure does not exhibit cylindrical symmetry in the $\boldsymbol{k}_t$-plane, the minibands do have nearly isotropic in-plane dispersion. Consequently, use of the axial approximation might seem justified, but the intersubband absorption would be almost zero if the γ_2- and γ_3-parameters were taken as equal, which is done in the axial approximation [11], as is further discussed below.

In order to explain the absorption spectra, we present in figure 4 the eigenfunctions at the centre of the superlattice Brillouin zone. The type of the state is indicated in the figure by the displayed non-zero component of the envelope function vector, the other ones being exactly zero at $k_t = 0$. Only one member of a doubly degenerate set of envelope functions is shown in figure 4, but it provides sufficient information on the role of symmetry in optical transitions.

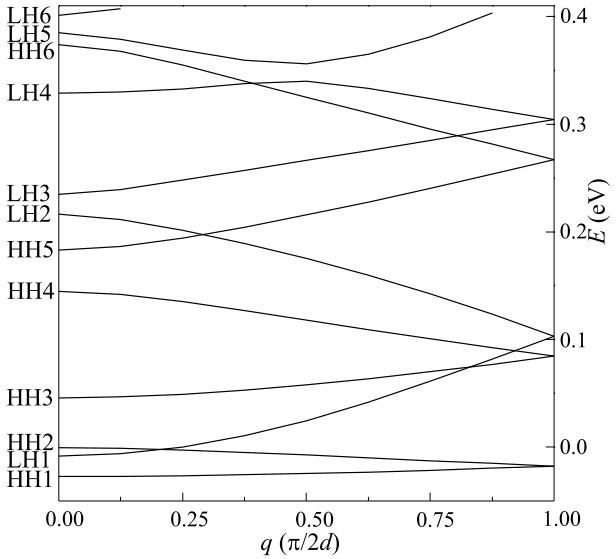

Figure 2. The miniband dispersion in the direction of the superlattice wave vector, at $k_t = 0$, in the $GaAs_9GaAs'_9$ twinning superlattice. There are six heavy-hole minibands in the energy range shown in the figure. Due to its low effective mass, the light-hole ground miniband (LH1) is wide enough to cross four HH minibands.

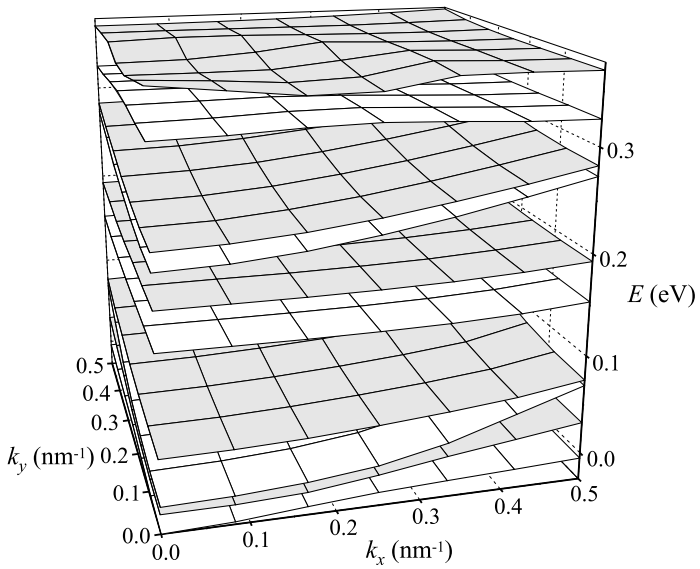

Figure 3. In-plane miniband dispersion in a $GaAs_9GaAs'_9$ twinning superlattice, at $q = 0$. Anticrossings between HH1 and LH1, and HH6 and LH4 minibands may be noticed.

States are classified as *normal* (with the wave-function periodicity equal to the superlattice half-period) and *folded* (with the periodicity of the superlattice full period), and their type is indicated in parentheses in figure 4, where n denotes a normal and f a folded state.

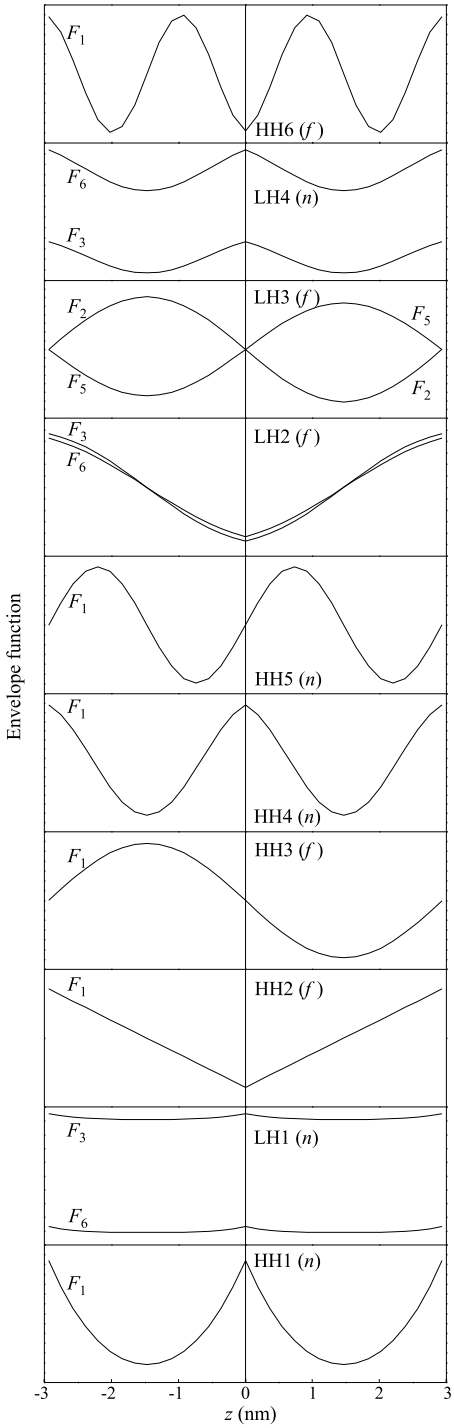

Figure 4. Wave functions at the Brillouin zone centre $k_t = 0$, $q = 0$. Only one member of the doubly degenerate set in the $GaAs_9GaAs'_9$ twinning superlattice is shown. The HH1 $\rightarrow$ LH2 transition is enabled by inversion of the dipole part of the matrix element C of the interaction Hamiltonian—opposite to what takes place in composite superlattices. In other words, the transition matrix element in this case is doubled, instead of vanishing.

Let us now consider the polarization dependence of the matrix elements and the absorption coefficient. For x-polarization and $k_t = 0$, coupling between minibands of different type and parity is enabled by dipole matrix elements B and C of the interaction Hamiltonian (table B1). However, of the two, only C is responsible for the dominant peak of the absorption coefficient. In other words, only the dipole part of C varies from one layer to the other, and the coupling is enabled between HH1 and LH2 minibands. In addition, a finite coupling arises from the change of the Luttinger parameters at two interfaces belonging to a superlattice period. The matrix element is more than halved in this way in GaAs in the centre of the 2D Brillouin zone; therefore this TSL exhibits relatively low absorption in the infrared part of the spectrum. The absorption of the z-polarized light is provided by the diagonal-matrix elements of the interaction Hamiltonian. Here the transitions occur between states of opposite parity but the same type (HH $\rightarrow$ HH), since the dipole parts of the diagonal-matrix elements extend unchanged throughout the $\boldsymbol{k}_t$-plane; therefore they act as the most effective terms. Because of that, the dominant transitions in GaAs are HH1 $\rightarrow$ HH5 and HH2 $\rightarrow$ HH3 transitions. Photon energies corresponding to these transitions are given in table 3(a). Inter-heavy-hole matrix elements are proportional to $\Gamma_z = \gamma_1 - 2\gamma_3$, which does not vary in the structure at all;

Table 3. Largest (in f) transition matrix elements $|M_{fi}|^2$ for the three lowest minibands in (a) GaAs, (b) Ge, and (c) Si TSLs, at $(k_x, k_y, q) = (0, 0, 0)$. Whether the transition is noticed in the absorption spectrum as a distinctive absorption line ('A. line') is indicated in the fourth column. For z-polarized light only the energies of the absorption lines (transition energies ΔE) are given. Types of state involved in the transitions (n or f) are indicated. All four combinations are allowed in TSLs, while coupling between n- and f-states is disabled in classical superlattices.

(a)

x-polarization				z-polarization	
Transition	$\lvert M_{fi}\rvert^2$ (nm^{-2})	ΔE (meV)	A. line	Transition	ΔE (meV)
HH1(n) $\rightarrow$ LH2(f)	0.532	244	yes	HH2(f) $\rightarrow$ HH3(f)	46
LH1(n) $\rightarrow$ HH2(f)	0.971	9	yes	HH1(n) $\rightarrow$ HH5(n)	210
HH2(f) $\rightarrow$ LH5(n)	9.51	385	no		
HH2(f) $\rightarrow$ LH3(f)	11.9	235	no		

(b)

x-polarization				z-polarization	
Transition	$\lvert M_{fi}\rvert^2$ (nm^{-2})	ΔE (meV)	A. line	Transition	ΔE (meV)
HH1(n) $\rightarrow$ LH2(f)	2.04	289	yes	HH1(n) $\rightarrow$ HH5(n)	384
LH1(n) $\rightarrow$ HH2(f)	2.86	29	yes		
HH2(f) $\rightarrow$ LH3(f)	8.09	247	no		

(c)

x-polarization				z-polarization	
Transition	$\lvert M_{fi}\rvert^2$ (nm^{-2})	ΔE (meV)	A. line	Transition	ΔE (meV)
HH1(n) $\rightarrow$ LH3(f)	0.143	131	yes	HH2(f) $\rightarrow$ HH3(f)	90
HH2(f) $\rightarrow$ LH2(n)	5.05	71	yes	HH1(n) $\rightarrow$ HH5(n)	309
HH2(f) $\rightarrow$ LH4(f)	0.0655	119	no		
HH2(f) $\rightarrow$ LH5(n)	11.3	296	yes		
LH1(n) $\rightarrow$ HH5(n)	0.0173	232	no		

that is, there are no interface terms in the transition matrix element. This combination of the Luttinger parameters amounts to 1.05 in GaAs. The momentum matrix element connecting heavy and light holes is now proportional to $\Gamma_x = 2\sqrt{2/3}(\gamma_2 - \gamma_3)$, which amounts to 1.14 in GaAs. This may lead one to conclude that the absorption coefficient attains about the same value for both x-polarized and z-polarized light. However, this is not so, because of the finite contribution of the interface terms in the case of x-polarization, as mentioned above. The resulting effect is about 2.5-times-lower absorption of x-polarized light than of z-polarized light. Even though the absorption peak for x-polarized light arises from the transition between the normal and the folded state, the matrix element associated with it may not be the largest one, as illustrated in table 3(a), where the largest (in f) squares of zone-centre matrix element moduli $|M_{fi}|^2$ for the three lowest initial minibands (i.e. $i = 1, 2, 3$) are given. Those responsible for the absorption lines in figure 5(a) are noted in the table. The matrix element connecting the

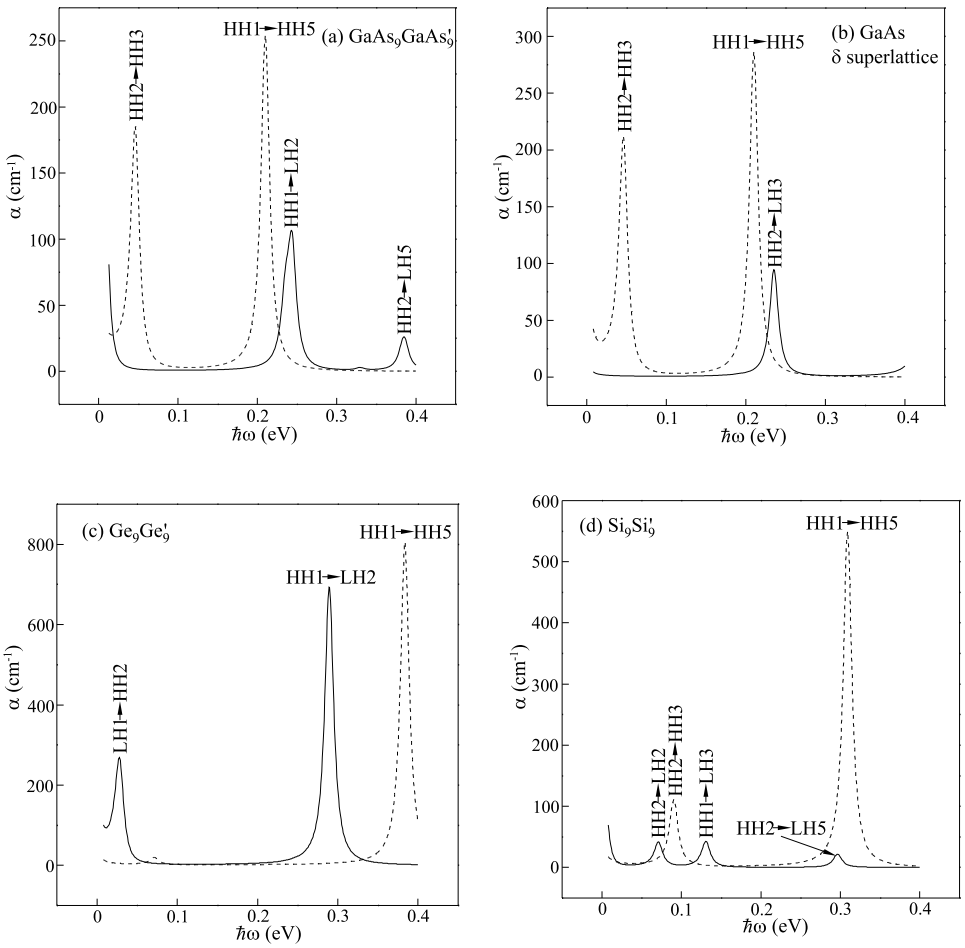

Figure 5. The absorption coefficients for (a) a GaAs twinning superlattice, (b) a fictitious GaAs δ-superlattice discussed in the text, (c) a Ge twinning superlattice, and (d) a Si twinning superlattice, for x-polarized light (solid lines) and for z-polarized light (dashed lines). The higher absorption of z-polarized light is due to the values of particular combinations of the Luttinger parameters that appear in the coupling terms.

HH2 and LH3 states, both of which are folded, is the strongest for the energy range chosen here. Nonetheless, it does not make a distinctive feature in the absorption spectrum, and is actually merged with the HH1 $\rightarrow$ LH2 transition. However, this folded-to-folded transition may dominate the spectrum for superlattices with wider layers, where HH2 would drop below LH1, and the absorption enhancement may occur due to both the increased population of the initial state and the increased matrix element. Due to the more rapidly varying envelope functions, the absorption coefficient should rise in thinner superlattices as well. However, use of the effective-mass theory can hardly be justified in this case, as is also noted by Wood and Zunger for the GaAs/AlAs system [24]. The issue of the dependence of the absorption on the layer thickness needs more thorough investigation. Finally, we should note that the wave functions and matrix elements all change with k_t, but it turns out that states with rather small k_t give the major contribution to the absorption, which implies that the properties of matrix elements as discussed above are directly reflected in the absorption profile.

In order to demonstrate the influence of the crystal rotation alone on the absorption spectrum, the absorption coefficient is also calculated for a hypothetical GaAs δ-superlattice, comprising layers of the same orientation, but with the δ-potential given by equation (11). The absorption of z-polarized light here occurs in transitions between the same states and has nearly the same magnitude as in twinning superlattices, as displayed in figures 5(a) and 5(b). In contrast, the absorption of x-polarized light is enabled by HH2 $\rightarrow$ LH3 transitions, where both states are folded. Hence the crystal rotation affects coupling between normal and folded states.

The influence of the band structure on the absorption in Ge and Si is illustrated in figure 5(c) and figure 5(d), respectively. Two absorption lines occurring upon HH1 $\rightarrow$ LH2 and LH1 $\rightarrow$ HH2 normal-to-folded transitions in Ge dominate the spectrum for x-polarized light. In spite of the larger matrix element for LH1 $\rightarrow$ HH2 transition and due to the population of the relevant states, the HH1 $\rightarrow$ LH2 absorption line is the strongest one. The HH2 $\rightarrow$ LH3 transition, offering an almost four-times-larger matrix element (table 3(b)), is not noticed in the spectrum, but for wider layers, the absorption on this transition may be dominant, as discussed above for the GaAs TSL. Both the initial and final state are folded here, and the eventual absorption line is enabled by the matrix element B of the interaction Hamiltonian. As previously mentioned, V_{SO} equals 0 for Ge and Si. This choice of the effective potential energy for SO holes implies that the SO band top should be reproduced as the eigenstate for $(k_x, k_y, q) = (0, 0, 0)$, with a constant envelope function in the superlattice. Nevertheless, one-to-one correspondence between envelope functions in two superlattices may be established for states higher than LH2 ($E = 44$ meV). For example, the shape of the components of the envelope function vector of the LH3 state in Si is the same as for the LH2 state in GaAs. Therefore the absorption line is due to HH1 $\rightarrow$ LH3 transition, but two additional lines appear in the spectrum (figure 5(d)), corresponding to folded-to-normal transitions. As for the comparison with Ge and GaAs, along with data for HH1 $\rightarrow$ LH3, HH2 $\rightarrow$ LH2, and HH2 $\rightarrow$ LH5 transitions, the values of the matrix elements of HH2 $\rightarrow$ LH4 and LH1 $\rightarrow$ HH5 transitions are given in table 3(c), but these are of no importance for the absorption due to the very low matrix elements. The combinations of Luttinger parameters enabling the absorption peak for two polarizations are larger for Ge and Si than for GaAs. For example, $\Gamma_z = 1.97$ and $\Gamma_x = 2.35$ for Ge, which implies four-times-stronger absorption in Ge than in GaAs. The ratio is even larger for x-polarized light, due to lower interface terms in the transition matrix element. For z-polarized light, the absorption is shifted to shorter wavelengths in $Ge_9Ge'_9$ TSLs, and is predominantly due to the HH1 $\rightarrow$ HH5 transition, whose energy is shown in table 3(b). In Si, the increase due to the bulk band structure ($\Gamma_x = 1.71$ and $\Gamma_z = 1.34$) is obscured by larger interface terms. Like for GaAs, these reduce the absorption coefficient of Si (for x-polarization so strongly that no peak exceeds 100 cm^{-1}). For z-polarized light, two

much higher peaks of the absorption coefficient, attributed to HH1 → HH5 and HH2 → HH3 transitions, are found for Si (table 3(c)).

In order to demonstrate the usefulness and limitations of the EMT, the absorption spectrum for the $Ge_6Ge'_6$ superlattice is also computed. One may doubt the validity of the EMT for layers as thin as this, but the EPM-based results were given in reference [3] for this case, and also for the Si-based TSL. Of the two, the Ge TSL shows better agreement between EMT- and EPM-calculated energies, as illustrated by table 2. The value $\Gamma = 10$ meV was chosen in the EPM calculation [3], and the same was used in this calculation, in order to provide a better assessment of the EMT results, and for the same reason EPM-calculated Luttinger parameters were used. The single peak of the absorption spectrum of the x-polarized light displayed in figure 6 is located at 52 meV and amounts to 1480 cm^{-1}, which compares favourably with the EPM-calculated values 58 meV and 1080 cm^{-1} (cf. figure 4(b) in reference [3]). The rather small deviations are due to the simplicity of the EMT. As for the longer-period $Ge_9Ge'_9$ superlattice, this peak originates from the LH1 → HH2 transition. Furthermore, the absorption spectrum calculated from the EPM for the z-polarized light has a peak at about the same energy as for the x-polarized light, and the peak value is about 400 cm^{-1}. According to EMT, however, the absorption coefficient does not exceed 1 cm^{-1} in the energy range 10–300 meV. More thorough inspection of EMT results shows that $|M_{fi}^{(z)}|^2$ for the dominant HH2 → HH3 transition is in fact more than 15 times larger than $|M_{fi}^{(x)}|^2$ for the LH1 → HH2 transition. This would give rise to a peak at about 82 meV, but it does not appear due to population effects. This indicates that the EMT-derived selection rules may be too strict, not predicting a transition found by microscopic EPM calculation, which is due to the relative simplicity of the former. Yet, the successful prediction of the main absorption feature in this case confirms the usefulness of the EMT.

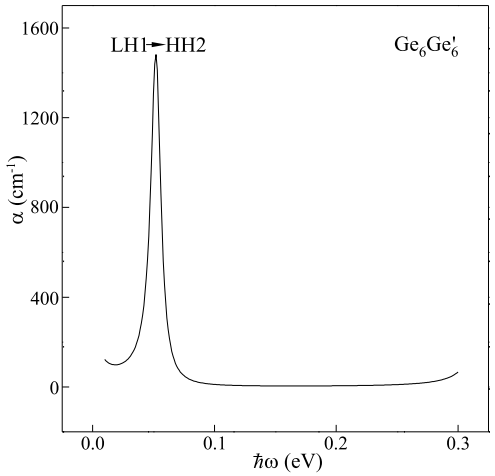

Figure 6. The absorption coefficient in the $Ge_6Ge'_6$ superlattice calculated for x-polarized light. Due to the strict selection rules, the peak of the z-polarized light found from the EPM is not reproduced by EMT, yet the displayed absorption peak compares favourably with the EPM result (reference [3]) in respect of both the location and the magnitude.

Finally we would like to point out that the consideration of the dependence of the absorption on the light polarization and material parameters is, to the best of our knowledge, novel and enabled by the relatively simple structure of the effective-mass Hamiltonian. Even though

results obtained from the EPM may be more reliable, they do not offer a straightforward account of the relationship between the superlattice electronic structure and the absorption spectrum.

5. Conclusions

Electronic structures of GaAs, Ge, and Si p-doped twinning superlattices are calculated using multiband effective-mass theory. A rather complex potential at the interface between two layers is approximated by a δ-potential allowed to vary in the set of eigenstates of the angular momentum, thus forming a diagonal-matrix potential, whose elements are found by fitting to the energy levels of a single twinning boundary as calculated using the empirical pseudopotential method. Good agreement with the pseudopotential calculation is achieved, in respect of both the eigenenergies in the zone centre and the miniband dispersion. In addition to the electronic structure, we calculated the intersubband absorption in these systems. As regards the polarization dependence of the absorption, our results support the findings of the pseudopotential theory [3], with deviations which are ascribed to the simplicity of the EMT. Miniband states between which the transitions occur, as well as the matrix elements of the interaction Hamiltonian responsible for the absorption, are indicated. The absorption peaks are explained by the structural parameters and the symmetries of the states taking part in the transitions. The strongest absorption is found in Ge, a lower value is calculated for Si, while a very small value, due to low in-plane anisotropy, is found for GaAs. The peculiar property of the twinning superlattice is the existence of coupling between *normal* heavy-hole and *folded* light-hole states. These transitions do not normally occur in composite microstructures, but are enabled by the crystal rotation in the twinning superlattice. Moreover, they give rise to the largest absorption peaks in all three semiconductors.

Appendix A. Boundary conditions

The boundary condition for the probability current density is obtained by integrating the system of differential equations represented by the Hamiltonian, equation (1), across the interface. In the considerations presented in this paper there appear two matrices of the same structure as the matrix in equation (1) (with $\Delta \to 0$), i.e.

$$D_{\text{eff}} = D_{2\downarrow}^{-1}(D_{1\uparrow} - D_{1\downarrow}) \tag{A.1}$$

$$D_{\delta} = D_{2\downarrow}^{-1} V_{\delta} \tag{A.2}$$

where $D_{1\uparrow}$, $D_{1\downarrow}$, and $D_{2\downarrow}$ are given in table A1.

Table A1. Matrices for the boundary condition, derived from the conservation of the probability current density. These matrices are composed analogously to the hole Hamiltonian; hence the same labels are used here as in equation (1).

Layer	P_{h}	Q_{h}	A_+	A_-	B	C
$D_{1\uparrow}$	0	0	0	0	$-\frac{\text{i}}{\sqrt{3}}(2\gamma_2 + \gamma_3)k_-$	$\text{i}\sqrt{\frac{2}{3}}(\gamma_2 - \gamma_3)k_+$
$D_{1\downarrow}$	0	0	0	0	$\frac{\text{i}}{\sqrt{3}}(2\gamma_2 + \gamma_3)k_-$	$-\text{i}\sqrt{\frac{2}{3}}(\gamma_2 - \gamma_3)k_+$
$D_{2\downarrow}$	γ_1	$-2\gamma_3$	$\gamma_1 - 2\gamma_3$	$\gamma_1 + 2\gamma_3$	0	0

Appendix B. The interaction Hamiltonian

The interaction Hamiltonian is obtained by finding a gradient of each element of the hole Hamiltonian, equation (1), in $\boldsymbol{k}$-space. Obviously, the Hamiltonian structure (with $\Delta \to 0$) is preserved, with only the matrix elements changed. These are displayed in table B1. The matrix elements appearing in these considerations are given by

$$\begin{aligned}
&\Pi_1 = 2\gamma_1 k_z && \Pi_2 = -4\gamma_3 k_z && \Pi_5 = 2(2\gamma_2 + \gamma_3)k_z \\
&\Pi_7 = 2(\gamma_1 - 2\gamma_3)k_z && \Pi_8 = 2(\gamma_1 + 2\gamma_3)k_z && \Pi_9 = 2(\gamma_2 - \gamma_3)k_z \\
&\Gamma_1 = 2\gamma_1 \qquad \Gamma_2 = 2\gamma_3 && \Gamma_3 = 2(\gamma_1 + \gamma_3) && \Gamma_4 = 2(\gamma_1 - \gamma_3) \\
&\Gamma_5 = 2(2\gamma_2 + \gamma_3) && \Gamma_6 = 2(\gamma_2 + 2\gamma_3) && \Gamma_9 = 2(\gamma_2 - \gamma_3).
\end{aligned} \tag{B.1}$$

Table B1. The matrix elements of the interaction Hamiltonian. At $k_t = 0$, the intersubband transitions for x-polarization are enabled by overlap terms, while for z-polarization the dipole interaction is the only one existing. The upper sign in the interface matrix $\mathcal{I}$ is for the $\uparrow$ layer, while the lower sign corresponds to the $\downarrow$ layer.

Layer	Polarization	P_h	Q_h	A_+	A_-	B	C
$\uparrow$	x	$\Gamma_1 k_x$	$\Gamma_2 k_x$	$\Gamma_3 k_x$	$\Gamma_4 k_x$	$\sqrt{\frac{2}{3}}\Gamma_9 k_+ - \frac{1}{\sqrt{3}}\Pi_5$	$-\frac{1}{\sqrt{3}}\Gamma_6 k_- + \sqrt{\frac{2}{3}}\Pi_9$
$\uparrow$	y	$\Gamma_1 k_y$	$\Gamma_2 k_y$	$\Gamma_3 k_y$	$\Gamma_4 k_y$	$-\mathrm{i}\sqrt{\frac{2}{3}}\Gamma_9 k_+ + \frac{\mathrm{i}}{\sqrt{3}}\Pi_5$	$\frac{\mathrm{i}}{\sqrt{3}}\Gamma_6 k_- + \mathrm{i}\sqrt{\frac{2}{3}}\Pi_9$
$\uparrow$	z	Π_1	Π_2	Π_7	Π_8	$-\frac{1}{\sqrt{3}}\Gamma_5 k_-$	$\sqrt{\frac{2}{3}}\Gamma_9 k_+$
$\downarrow$	x	$\Gamma_1 k_x$	$\Gamma_2 k_x$	$\Gamma_3 k_x$	$\Gamma_4 k_x$	$-\sqrt{\frac{2}{3}}\Gamma_9 k_+ - \frac{1}{\sqrt{3}}\Pi_5$	$-\frac{1}{\sqrt{3}}\Gamma_6 k_- - \sqrt{\frac{2}{3}}\Pi_9$
$\downarrow$	y	$\Gamma_1 k_y$	$\Gamma_2 k_y$	$\Gamma_3 k_y$	$\Gamma_4 k_y$	$\mathrm{i}\sqrt{\frac{2}{3}}\Gamma_9 k_+ + \frac{\mathrm{i}}{\sqrt{3}}\Pi_5$	$\frac{\mathrm{i}}{\sqrt{3}}\Gamma_6 k_- - \mathrm{i}\sqrt{\frac{2}{3}}\Pi_9$
$\downarrow$	z	Π_1	Π_2	Π_7	Π_8	$-\frac{1}{\sqrt{3}}\Gamma_5 k_-$	$-\sqrt{\frac{2}{3}}\Gamma_9 k_+$
$\mathcal{I}$	x	0	0	0	0	0	$\pm\sqrt{\frac{2}{3}}\Gamma_9$
$\mathcal{I}$	y	0	0	0	0	0	$\pm\mathrm{i}\sqrt{\frac{2}{3}}\Gamma_9$
$\mathcal{I}$	z	0	0	0	0	0	0

References

[1] Zhang Y and Mascarenhas A 1997 *Phys. Rev.* B **55** 13 100
[2] Ikonić Z, Srivastava G P and Inkson J C 1993 *Phys. Rev.* B **48** 17 181
[3] Ikonić Z, Srivastava G P and Inkson J C 1995 *Phys. Rev.* B **52** 14 078
[4] Ikonić Z, Srivastava G P and Inkson J C 1997 *Phys. Rev.* B **55** 9286
[5] Hofmeister H, Bardamid A F, Janghanns T and Nepijko S A 1991 *Thin Solid Films* **205** 20
[6] Hiruma K, Yazawa M, Haraguchi K and Ogawa K 1993 *J. Appl. Phys.* **74** 3162
[7] Hibino H, Sumimoto K and Ogino T 1998 *J. Vac. Sci. Technol.* A **16** 1934
[8] Luttinger J M and Kohn W 1955 *Phys. Rev.* **97** 869
Luttinger J M 1956 *Phys. Rev.* **102** 1030
[9] Seidl A, Görling A, Vogl P, Majewski J A and Levy M 1996 *Phys. Rev.* B **53** 3764
[10] Chao C Y-P and Chuang S L 1992 *Phys. Rev.* B **46** 4110
[11] Ikonić Z, Milanović V and Tjapkin D 1992 *Phys. Rev.* B **46** 4285
[12] Chou M Y, Cohen M L and Louie S G 1985 *Phys. Rev.* B **32** 7979
[13] Murayama M and Nakayama T 1994 *Phys. Rev.* B **49** 4710
[14] Liu H C 1987 *Appl. Phys. Lett.* **51** 1019
[15] Edwards G, Valadares E C and Sheard F W 1994 *Phys. Rev.* B **50** 8493

[16] Szmulowicz F 1996 *Phys. Rev.* B **54** 11 539
[17] Foreman B A 1997 *Phys. Rev.* B **56** R12 748
[18] Stoklitsky S A, Holtz P O, Monemar B, Zhao Q X and Lundström T 1994 *Appl. Phys. Lett.* **65** 1706
[19] Szmulowicz F and Brown G J 1995 *Appl. Phys. Lett.* **66** 1659
[20] Ikonić Z, Milanović V and Tadić M 1995 *J. Phys.: Condens. Matter* **7** 7045
[21] Bockelmann U and Bastard G 1992 *Phys. Rev.* B **45** 1688
[22] Madelung O (ed) 1991 *Semiconductors, Group IV Elements and III–V Compounds* (Berlin: Springer)
[23] Hinckley J M and Singh J 1990 *Phys. Rev.* B **42** 3546
[24] Wood D M and Zunger A 1996 *Phys. Rev.* B **53** 7949